


## Article

# Electrochemical Aptasensor Based on ZnO-Au Nanocomposites for the Determination of *Ochratoxin A* in Wine and Beer

Sai Zhang <sup>1</sup>, Yahui Wang <sup>2</sup>, Qinglin Sheng <sup>2,\*</sup>  and Tianli Yue <sup>2,\*</sup>

<sup>1</sup> Key Laboratory of Shaanxi Administration of Traditional Chinese Medicine for TCM Compatibility, Shaanxi University of Chinese Medicine, Xi'an 712046, China; zhangsai@sntcm.edu.cn

<sup>2</sup> College of Food Science and Technology, Northwest University, Xi'an 710069, China

\* Correspondence: qlsheng@nwu.edu.cn (Q.S.); yuetl@nwu.edu.cn (T.Y.)

**Abstract:** *Ochratoxin A* (OTA) is positively correlated with an increased risk of developing cancer in nephrotoxic and hepatotoxic patients. Therefore, it is of great significance for the highly sensitive, highly selective, and timely detection of OTA. We described here an electrochemical aptasensor for OTA analysis, which took advantage of the favorable properties of gold nanoparticles (AuNPs) functionalized zinc oxide (ZnO) composites and the intercalative binding between methylene blue (MB) and nucleic acid. There were two label-free aptamers: one to capture OTA and another serving as complementary DNA (cDNA), enabling connection to the ZnO-Au composite's immobilized electrode. Once OTA was present, the aptamer could capture OTA and detach from the electrode interface, thus, preventing MB from accessing electrode surface for efficient electron transfer; a decreased peak current was monitored by differential pulse voltammetry. The aptasensor presented nice analytical performance for OTA detection in the range of 0.1–30,000 pg·mL<sup>-1</sup>, with a detection limit of 0.05 pg·mL<sup>-1</sup>. Moreover, the developed biosensor could be applied to actual sample (wine and beer) analysis.

**Keywords:** food safety; electrochemical aptasensor; intercalative binding; zinc oxide-gold composites; *Ochratoxin A*



**Citation:** Zhang, S.; Wang, Y.; Sheng, Q.; Yue, T. Electrochemical Aptasensor Based on ZnO-Au Nanocomposites for the Determination of *Ochratoxin A* in Wine and Beer. *Processes* **2023**, *11*, 864. <https://doi.org/10.3390/pr11030864>

Academic Editors: Dariusz Dziki, Francesca Blasi, Won Byong Yoon, Akiyoshi Sawabe and Beata Biernacka

Received: 21 February 2023

Revised: 11 March 2023

Accepted: 12 March 2023

Published: 14 March 2023



**Copyright:** © 2023 by the authors. Licensee MDPI, Basel, Switzerland. This article is an open access article distributed under the terms and conditions of the Creative Commons Attribution (CC BY) license (<https://creativecommons.org/licenses/by/4.0/>).

## 1. Introduction

As a mycotoxin, *Ochratoxin A* is produced by *Aspergillus* and *Penicillium* under suitable conditions and was first discovered in South Africa in 1965 [1]. Mycotoxins are mainly *Ochratoxin A*, *Ochratoxin B*, and *Ochratoxin C*, among which OTA is most commonly detected and has the highest toxicity [2]. The primary sources of OTA are food commodities such as cereal grains (corn), dairy products, coffee beans, raisins, wine, fruits, vegetables (garlic, yam, potatoes, onions, and tomatoes), and spices [3]. Moreover, OTA is difficult to completely remove in food storage and processing due to its strong thermal and chemical stability. Human ingestion of OTA-infected food may produce renal toxicity, hepatotoxicity, teratogenicity, and immunotoxicity. In order to reduce the adverse effects of OTA on human body, the Food Safety Organization of China has set strict limit standards for OTA content in food [4]: wine ( $\leq 2 \mu\text{g}\cdot\text{kg}^{-1}$ ); grain and its products, beans, roasted coffee beans and roasted coffee ( $\leq 5 \mu\text{g}\cdot\text{kg}^{-1}$ ); soluble coffee ( $\leq 10 \mu\text{g}\cdot\text{kg}^{-1}$ ). Thus, the timely detection of OTA is of great significance. Currently, the main methods used to detect OTA are fluorimetric-visual assay [5], chromatography-tandem mass spectrometry [1], high performance liquid chromatography-fluorescence [6], enzyme linked immunosorbent assay [7], and electrochemical method [8]. Most sensors are time-consuming and rely on expensive equipment, professional technicians, and complex pretreatment processes, and are not suitable for field diagnosis of mycotoxins. Fortunately, electrochemical sensors, with the merits of being highly sensitive, easy to operate, and easy to miniaturize, have broad application prospects for the rapid detection of food contaminants.

Bioactive and bioactive free-based electrochemical sensors have been used to detect estrogens, glucose, toxins, and pathogenic bacteria in food. The mechanism of an electrochemical sensor is mainly composed of two parts: (1) Recognition by interaction with the analyte; (2) Transduction, that is, when the interaction is converted into a readable signal [9]. The recognition or sensing element must be sensitive and specific to the detected object. An electrochemical biosensor takes a bioactive unit (such as an enzyme, antibody, nucleic acid, aptamer, etc.) as the recognition element, combined with a chemical and physical conversion element (such as an electrode), and has high selectivity and sensitivity to the specific analyte [9]. Compared with non-bioactive sensors, biosensors have the advantage of high selectivity due to the existence of specific recognition elements. Moreover, biosensors play a key role in the detection of biomolecules or their metabolites, and could achieve high sensitivity, high accuracy, rapid, semi-automatic, and fully automated analysis.

As mentioned above, sensitivity is one of the crucial analytical properties of biosensors. How to promote the sensitivity of biosensors remains a problem worth studying. The researchers mainly used featured materials [10], unique nucleic acid structure [8], nucleic acid amplification [11], and other signal amplification strategies to improve the sensitivity of the sensor. Among these strategies, novel materials have been extensively applied to sensing systems due to their excellent performance. There are commonly-used, in-sensor novel materials including carbon-based materials, conducting polymers, covalent organic frameworks, metal-organic frameworks, and metal oxides [12–16]. Although most materials, especially nanostructured materials, have high specific surface areas that provide more binding sites, their electrical conductivity is poor. The defects of a single material can be overcome by the combination of two or more materials. At the present stage, transition metal oxides are cost-effective and abundant materials, and can form composites with noble metals that display excellent selectivity when coupled to biorecognition elements [17]. Zinc oxide (ZnO) has broad prospects in energy conversion and storage, photoelectricity, and environmental remediation [18]. Bio-acceptable 0D and 1D ZnO nanostructures, as sensors and assay platforms, have offered biomolecular selectivity and sensitivity for cancer diagnosis and treatment and are going to emerge as breakthrough candidates for the medical field [19]. Das et al. [20] researched the interaction of a fluorescent ZnO-Au nanocomposite with deoxyribonucleic acid. The result indicated that the designed ZnO-Au can be used as a fluorescent probe for nanomaterial-based DNA-binding study and to distinguish, skillfully, between single-stranded DNA and double-stranded DNA. ZnO-Au nanocomposites were also prepared for high-performance supercapacitors [21]. The nanocomposites can be considered to be the most promising materials for the next generation of supercapacitors due to their high specific capacitance and good cycle stability. Yao et al. [22] synthesized powdered ZnO-Au nanocomposites through a facile and controlled method. The ZnO-Au nanocomposites exhibited excellent photocatalytic stability and can be reusable as photocatalysts.

Aptamers (mainly DNA and RNA) are screened from nucleotide libraries through the in vitro technology of exponential enrichment ligand phylogeny and have high specificity for target molecules such as ions, antibiotics, proteins, and even the whole cell [23]. Aptamers have become a promising molecular recognition tool in biosensors due to their essential characteristics of small size, low cost, high sensitivity, high selectivity and high stability [24]. Although aptamers labeled by various functional groups or electroactive molecules are also easily synthesized, labeling techniques will reduce the affinity of the aptamers and increase the economic cost. Zhao et al. [25] utilized two aptamers labeled with electroactive molecules to determinate patulin and OTA, respectively. *Patulin* and *OTA* can be quantified at a linearity range of  $10^{-9}$ – $0.1 \mu\text{g}\cdot\text{mL}^{-1}$ . Compared to labeled aptamers, label-free aptamers with sandwich structure presented higher affinity for the target. For example, the simultaneous use of two DNA aptamers for capturing thrombin is a very powerful way to enhance the selectivity of sensing systems [26]. However, sandwich structure requires two aptamers to bind to different sites, which is a complex and time-

consuming operation. Therefore, researchers pay attention to the development of label-free sensors based on targets-induced chain displacement.

With an effort to develop targets-induced, chain-displacement-based analysis, we designed a highly sensitive aptasensor reliant on flower ZnO-Au composites and methylene blue interaction with nucleic acid. In the presence of OTA, the original double-stranded DNA on the electrode surface becomes single-stranded DNA, affecting the binding of electroactive molecules with nucleic acids. We showed an application of targets-induced chain displacement assay to the detection of OTA in wine and beer samples.

## 2. Experimental Section

### 2.1. Reagents

The main following reagents were used as received (all reagent grade): Zinc nitrate ( $\text{Zn}(\text{NO}_3)_2 \cdot 6\text{H}_2\text{O}$ ,  $\geq 99.0\%$ , Shanghai Aibi Chemical Reagent Co., Ltd. Shanghai, China); Chloroauric acid ( $\text{HAuCl}_4 \cdot 4\text{H}_2\text{O}$ , 99%, Shanghai Chemical Reagent Co., Ltd. Shanghai, China); Tris(hydroxymethyl)aminomethane (Tris-HCl,  $>99.9\%$ , Shanghai Sangon Bio-engineering Co., Ltd. Shanghai, China); Methylene blue trihydrate (MB, Tianjin Kermel Chemical Reagent Co., Ltd. Tianjin, China); 6-mercapto-1-hexanol (MCH, 97%), Tris-(2-carboxyethyl) phosphine hydrochloride (TCEP,  $\geq 98.0\%$ ) and Perfluorosulfonic acid-PTFE copolymer (Nafion, 5%) were obtained from Sigma Aldrich Shanghai Co., Ltd (Shanghai, China); Ethylenediaminetetraacetic acid (EDTA, 99.5%), *Ochratoxin A* (OTA, 98%), *Zearalenone* (ZEA), *Patulin* (PAT), and *Deoxynivalenol* were purchased from Shanghai Aladdin Biochemical Technology Co., Ltd (Shanghai, China).

TE buffer (pH = 8) mainly consisted of 10 mM Tris-HCl and 1 mM EDTA. Ultrapure water (UP  $> 18.25 \text{ M}\Omega \cdot \text{cm}@25^\circ\text{C}$ ) was obtained from an ultrapure water machine system and used throughout the experiments. Complementary DNA (cDNA, 5'-SH-( $\text{CH}_2$ )<sub>6</sub>-T-40-T-CAC CCA CAC CCG ATC CTC AGC-3'), aptamer-OTA (aptamer, 5'-TGA GGA TCG GGT GTG GGT GGC GTA AAG GGA GCA TCG GAC A-3'), BHQ2-aptamer-OTA, and Cy3-cDNA were purchased from Takara Biotechnology (Beijing) Co., Ltd. (Beijing, China).

### 2.2. Apparatus

Scanning electron microscopy (SEM) was used to characterized the morphology, layered structure, and size of ZnO-Au composites. SEM images were obtained using a SU8010 instrument produced by Nippon Corporation, Japan. Samples were suspended in ultrapure water and dispersed onto square, single-polished silicon wafers ( $3 \times 3 \text{ mm}$ ) at a thickness of 0.725 mm.

Fourier transform infrared spectrometer (FTIR, TENSOR27, Brooke, Germany) was used to characterize functional groups on the surface of samples in the range of 400–4000  $\text{cm}^{-1}$ . Powder samples were mixed well with KBr and pressed into coin-shaped pellets for testing.

UV-visible absorption spectrum (UV-vis) was measured with an Agilent Cary-100 spectrophotometer (Agilent technology, America) at room temperature.

X ray powder diffractometer (XRD, D8 ADVANCE, Brooke, Karlsruhe, Germany) data was recorded using graphite-monochromatic  $\text{Cu-K}\alpha$  radiation. Powder samples were scanned with a 2-Theta range from 20 to 80 degree at a step width of 0.05 degree.

X-ray photoelectron spectroscopy (XPS, Ulvac-Phi, Kanagawa, Japan) was carried out on a PHI 5000 Versaprobe III spectrometer with the calibrated C1s peak of 284.8 eV. The samples preparation process was the same as SEM.

Fluorescence intensities were recorded on a F-4500 spectrofluorimeter (Hitachi, Japan). The emission spectra were recorded within the wavelength range of 500–640 nm upon excitation at 490 nm.

Electrochemical measurements (electrochemical impedance spectroscopy, EIS, and differential pulse voltammetry, DPV) were carried out on a CHI 660D electrochemical workstation (Shanghai Chenhua Instrument Co., Ltd., Shanghai, China) using a three-electrode electroanalysis system. The three-electrode system consisted of a working electrode (glassy carbon electrode, GCE, diameter = 3 mm), reference electrode (saturated silver/silver

chloride), and auxiliary electrode (platinum filament). EIS was performed under initial potential of 0.27 V (versus Ag/AgCl) in a frequency range of 100 kHz to 0.1 Hz, with amplitude of 0.005 V and quiet time of 2 s. DPV was also implemented through setting the scan potential range (−0.7 V to 0.1 V versus Ag/AgCl) and sensitivity ( $1 \times 10^{-6}$  A/V), defaulting other parameters such as potential increment of 0.004 V, amplitude of 0.05 V, pulse width of 0.05 s, sample width of 0.0167 s, pulse period of 0.5 s, and quiet time of 2 s.

### 2.3. Fabrication of Aptasensor

#### 2.3.1. Preparation of Flower-like ZnO-Au Composites

ZnO flower and AuNPs-functionalized ZnO flower were synthesized in an alkaline and acid aqueous solution, respectively, by a modified reported method [27]. In the ZnO flower synthesis process, 10 mL of  $0.5 \text{ mol}\cdot\text{L}^{-1}$  zinc nitrate aqueous solution was added into 10 mL of  $4 \text{ mol}\cdot\text{L}^{-1}$  KOH aqueous solution drop by drop under continuous magnetic stirring. The obtained solutions maintained  $30 \text{ }^\circ\text{C}$  for 12 h under continuous magnetic stirring. White ZnO flower could be attained through washing products using ethanol and drying.

In addition,  $586 \text{ }\mu\text{L}$  of  $10 \text{ mg}\cdot\text{mL}^{-1}$  chloroauric acid and 1 mL methanol were added into 20 mL ultrapure water. The pH of mixed solution was adjusted to near neutral using  $0.01 \text{ mol}\cdot\text{L}^{-1}$  NaOH under stirring. 30 mg of ZnO powder was then added to the neutral solution and stirred for 1 h. The total solution was transferred to a stainless-steel autoclave and kept at  $120 \text{ }^\circ\text{C}$  for 1 h. After being slowly cooled down to room temperature, the samples were collected by centrifugation and washed with ethanol and ultrapure water, and then dried to obtain purple–red ZnO-Au composites.

#### 2.3.2. Aptasensor Development

GCE, after being polished via  $\text{Al}_2\text{O}_3$  powder with a diameter of  $0.05 \text{ }\mu\text{m}$ , was immersed in ethanol and water solution for ultrasonic cleaning. The cleaned electrode was dried with nitrogen gas for later use. 1 mg of prepared ZnO-Au composites were uniformly dispersed in 1 mL of ultrapure water to obtain purple suspension ( $1 \text{ mg}\cdot\text{mL}^{-1}$ ). Then,  $6 \text{ }\mu\text{L}$  suspension was dripped onto the electrode and dried at room temperature. At last, nafion@ZnO-Au/GCE membrane was formed after  $4 \text{ }\mu\text{L}$  nafion solution (0.5%) dripped on ZnO-Au composites modified GCE. Here, nafion was used not only as an immobilizing binder that produced uniform composite film, but also a filtering membrane in electroanalytical applications to improve selectivity of the sensor.

The electrode prepared above was used to conduct a series of incubation processes for OTA analysis. Before immobilization, cDNA and aptamer were denatured via heating at  $95 \text{ }^\circ\text{C}$  for 5 min and then ice-cooled for 5 min. First,  $6 \text{ }\mu\text{L}$  of  $1 \text{ }\mu\text{mol}\cdot\text{L}^{-1}$  cDNA (including  $0.05 \text{ mM}$  TCEP in  $\text{pH} = 8.0$  TE buffer) was dripped onto the prepared electrode and kept under high humidity at room temperature overnight. Next, the modified surface was rinsed with buffer solution and then passivated with  $1 \text{ mmol}\cdot\text{L}^{-1}$  MCH in Tris-HCl buffer ( $\text{pH} = 7.4$ ) for 1 h. After washing,  $6 \text{ }\mu\text{L}$  of  $1 \text{ }\mu\text{mol}\cdot\text{L}^{-1}$  aptamer was dropped on the above electrode and incubated for 2 h for specific base pairing. After that, the modified electrode was immersed in  $20 \text{ }\mu\text{mol}\cdot\text{L}^{-1}$  MB solution and maintained for an appropriate time. Finally, the modified electrode was cleaned with Tris-HCl buffer and dried to obtain MB/aptamer/MCH/cDNA/nafion@ZnO-AuNPs/GCE.

#### 2.4. Electrochemical Detection

Differential pulse voltammetry was performed in 10 mL Tris-HCl buffer (pH = 7.4) in a potential range of  $-0.7$  V to  $0.1$  V (versus Ag/AgCl). Prior to differential pulse voltammetric measurement, the modified electrode was incubated in Tris-HCl buffer containing OTA for an appropriate time. The concentration of OTA was quantified through the reduction peak current of MB.

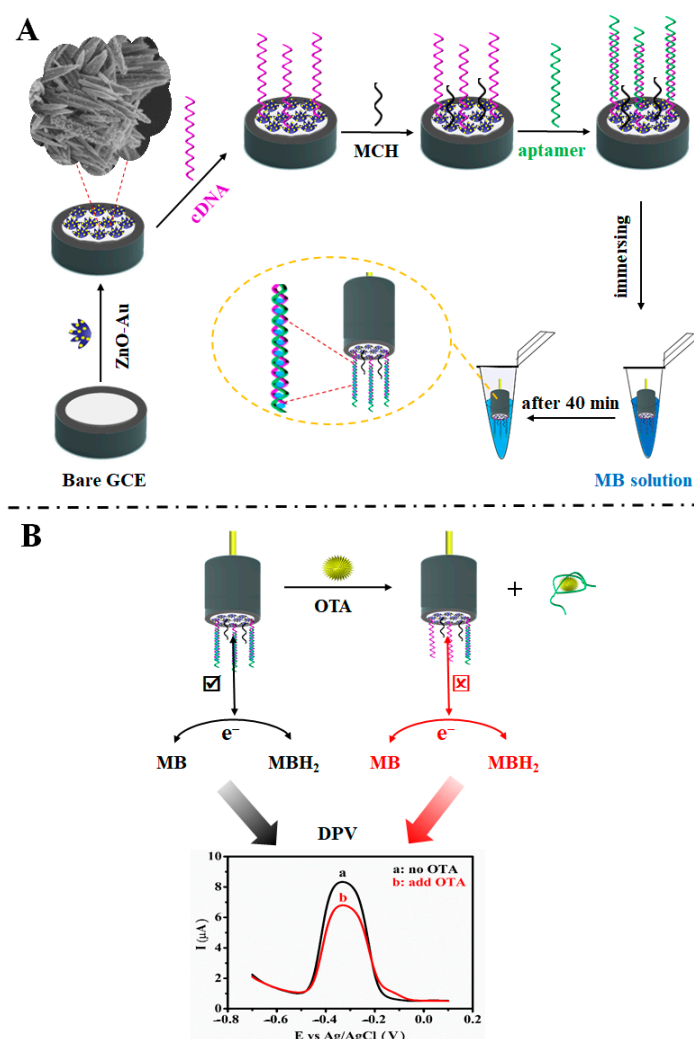
#### 2.5. Real Sample Analysis

Wine and beer samples, obtained from a local store, were degassed with nitrogen gas before being applied to electrochemical analysis. Testing was performed by spiking OTA into samples at a series of concentrations of  $0.1$ ,  $1$ ,  $100$ , and  $1000$   $\text{pg}\cdot\text{mL}^{-1}$ .

### 3. Results and Discussion

#### 3.1. Principle of the OTA Aptasensor

The OTA aptasensor described herein was used to detect OTA by integrating ZnO-Au composites and nucleic acid interaction with MB. Sulfhydryl-labeled cDNA was linked to a ZnO-Au modified electrode via Au-S covalent bond. Double-strand DNA (dsDNA) was obtained by the complementation of aptamer and single-strand DNA (ssDNA or cDNA). MB attached to dsDNA via intercalative binding to generate high peak current [28], due to the electron transfer of MB/MBH<sub>2</sub> (MBH<sub>2</sub>: reduced state of MB) on electrode sensing surface. Once OTA was present, the aptamer could capture OTA and detach from the electrode interface. Then, the double-strand DNA (dsDNA) was changed to single-strand DNA (ssDNA). In this case, the MB molecules would have detached from the dsDNA and released into the solution, preventing MB/MBH<sub>2</sub> from accessing the electrode surface for efficient electron transfer; a weak peak current of MB was obtained. The changes in peak current dependency, with the scan rate before and after the release of MB, further proved that the electrode reaction changed from a surface-controlled process to a diffusion-controlled one (Figure S1). DPV with the scan potential range of  $-0.7$  V to  $0.1$  V (versus Ag/AgCl) could be used to detect the reduction peak of MB. The entire fabrication and sensing application of the developed biointerface is illustrated in Scheme 1.



**Scheme 1.** Schematic illustration of the fabrication steps: (A) Sensing roadmap; (B) OTA sensing based on ZnO-Au composites/apptamer assembled on GCE.

Due to aptamer-specific capture OTA, the original dsDNA on the electrode is changed into ssDNA, which affects the binding of MB with nucleic acid. MB is one of the most commonly used cationic dyes and is easily detected via UV-vis. Thus, UV-vis was used to investigate MB in different systems. The aqueous solution of MB had a strong absorption peak at 664 nm, which was assigned to MB monomer (Figure S2). The other acromion at about 613 nm belonged to MB dimer [29]. After intercalating of the MB into DNA (dsDNA or ssDNA), the absorption intensity of the MB monomer was weakened and accompanied by a slight redshift. This effect was attributed to intercalative binding of MB and bases. Both MB and DNA molecules contain unique aromatic structures. When the  $\pi$  electrons of two molecules were combined, the empty  $\pi^*$  orbital (MB) was coupled to the  $\pi$  orbital (base), thereby decreasing the required energy for the  $\pi-\pi^*$  electron transition, which resulted in a redshift. At the same time, the empty  $\pi^*$  orbital was partially filled with electrons, which reduced the probability of  $\pi-\pi^*$  transition and weakened the absorption intensity [30]. Significantly, compared with the combination of MB and ssDNA, the intercalative binding between MB and dsDNA was stronger than the binding of MB and ssDNA. The principle of the designed aptasensor is based on the target-object induced chain displacement, which leads to the change in the number of electroactive molecules on the sensing interface.



### 3.2. Characterization of Composites and Modified Electrode

The SEM microstructure of the materials obtained from hydrothermal reaction is presented in Figure 1A–D. The ZnO material was comprised of a great many hierarchical, flower-like structures with an array of oriented, tapered branches (Figure 1A). Each tapered petal with an extremely smooth surface was in the length of 1–2  $\mu\text{m}$  (Figure 1B). The SEM micrographs of ZnO-Au hybrids were shown in Figure 1C,D. The local view of magnified SEM image (Figure 1D) revealed that spherical gold nanoparticles had been successfully attached to ZnO materials. It was obvious that the tapered-branches morphology of ZnO appeared marginally coarsened after the attachment of gold nanoparticles (AuNPs), leading to a decrease in length and width, which could be the corrosion effect of chloroauric acid. Because the surface roughness of materials is positively related to its specific surface area, the obtained ZnO-Au composites provide larger surface area to promote the electron transfer in electrochemical sensing systems.

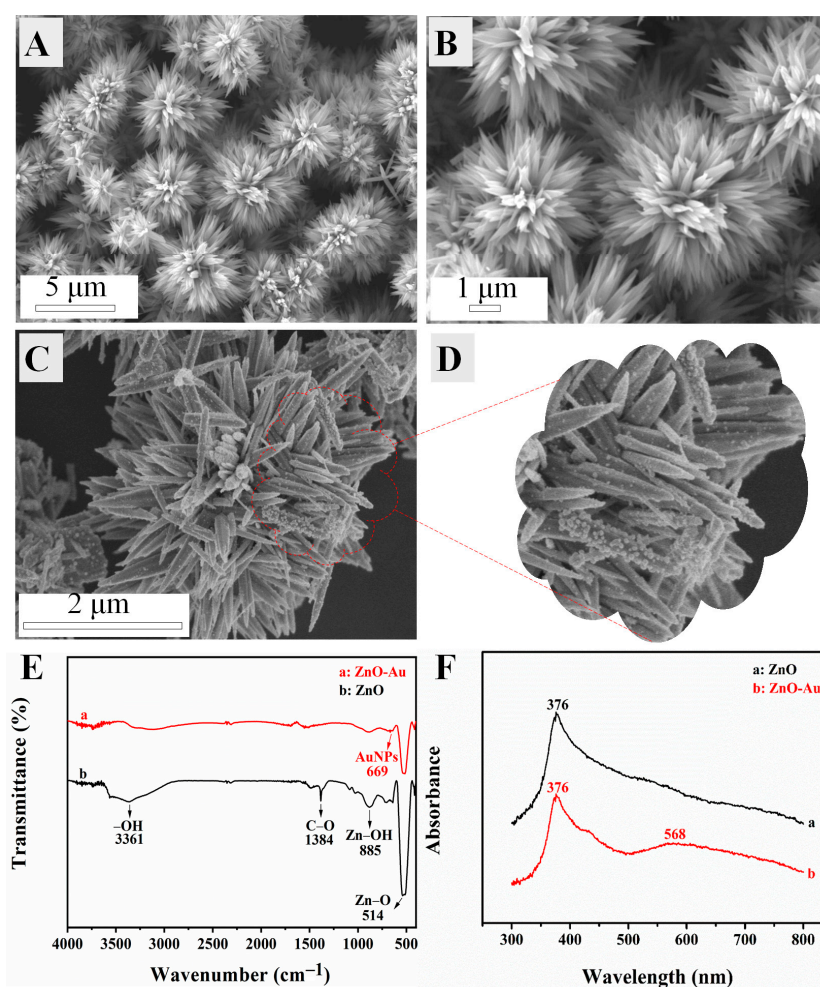


**Figure 1.** (A,B) SEM images of ZnO materials at low and high magnification; (C) SEM images of ZnO-Au composites; (D) Local magnification image of ZnO-Au composites; (E) FTIR spectra and (F) UV-visible absorption spectra of ZnO flowers and ZnO-Au composites.

ZnO flower and ZnO-Au composites were evaluated by FTIR and UV-vis. The FTIR spectra of ZnO and ZnO-Au composites were recorded in Figure 1E. The pure ZnO flower presented a sharp characteristic band at 514  $\text{cm}^{-1}$  from the stretching of Zn-O. The stretching modes of Zn-OH and C-O groups were observed at 885  $\text{cm}^{-1}$  and 1384  $\text{cm}^{-1}$ , respectively. The bands at 3361  $\text{cm}^{-1}$  corresponded to the stretching and bending vibrations of the O-H group. The profile of the ZnO-Au NPs displayed a slight peak at 669  $\text{cm}^{-1}$  due

to the attachment of AuNPs to ZnO flower [21]. There was a slight change in the peaks, which confirmed the coverage of ZnO by AuNPs. The UV-vis absorption spectra of ZnO flower and ZnO-Au composites were presented (Figure 1F), such as a sharp peak around 376 nm due to the excitonic absorption of ZnO and the broad hump around 568 nm of Au because of the surface plasmon resonance. The main absorption in the composites occurred in ZnO rather than gold, due to the low concentration of AuNPs in the composites as well as the high absorbance of ZnO. Moreover, a slight decrease in the absorption intensity at about 376 nm was observed for the ZnO-Au composites, which indicated the presence of AuNPs on the ZnO surface [31]. The UV-vis results further demonstrated the associative interaction between ZnO flower and AuNPs, which was consistent with the results of the FTIR spectra.

Impedance characterization was used to compare the electrical conductivity of electrode materials using  $[\text{Fe}(\text{CN})_6]^{-3/-4}$  as a redox probe (Figure S3A). According to Randle theory [32], the electrolytic cell can be simulated to obtain the model circuit including charge-transfer resistance ( $R_{ct}$ ), Warburg impedance ( $Z_w$ ), solution resistance ( $R_s$ ), and double-layer capacitance ( $C_d$ ). In the Nyquist plots, semicircle diameter and straight line corresponds to  $R_{ct}$  and  $Z_w$ , respectively. The  $R_{ct}$  values are obviously different during modification of different materials on the electrode surface. It can be seen that the  $R_{ct}$  value of 345  $\Omega$  for bare GCE showed a high electron transfer behavior between the electrode interface and redox probe. The  $R_{ct}$  value of the electrode interface increased to 598  $\Omega$  after the modification of ZnO on the GCE, due to relatively poor conductivity of ZnO. The ZnO-Au composites modified GCE presented a lower  $R_{ct}$  (448  $\Omega$ ), when compared with ZnO modified GCE (598  $\Omega$ ), owing to the strong electrical conductivity of AuNPs. The effective electrode surface areas were also investigated by recording the anodic and cathodic peak currents of different electrodes at a scan rate of 50 mV/s. The effective electrode surface areas in each case were determined based on the Randle-Sevcik equation [33]. The effective surface area of ZnO-Au and ZnO bare GCE were found to be 0.071 cm<sup>2</sup> and 0.056 cm<sup>2</sup>, respectively, compared to 0.034 cm<sup>2</sup> for bare GCE. Therefore, ZnO-Au composites/GCE with larger surface area and high electrical conductivity can be used to fabricate electrochemical aptasensors.

XRD patterns for 2-Theta values between 20–80° for ZnO and ZnO-Au samples sintered in air and argon are shown in Figure 2A. The diffraction peaks of ZnO-Au composites were completely consistent with the standard cards of ZnO (JCPDS No. 75-0576) and Au (JCPDS No. 01-1172), which indicated the successful synthesis of ZnO-Au with pure phase products. The XRD patterns of ZnO showed that the peaks at 31.84°, 34.502°, 36.336°, 47.652°, 56.73°, 63.014°, 66.54°, 68.118°, 69.259°, 72.757°, and 77.16° corresponded to the crystal faces of (100), (002), (101), (102), (110), (103), (200), (112), (201), (004), and (202), respectively. Besides, there were diffraction peaks at 38.268°, 44.599°, 64.677°, and 77.547° which, respectively, corresponded to (111), (200), (220), and (311) crystal faces of Au. As far as the (101) plane of ZnO crystals is concerned, it is a nonpolar surface and its surface energy is higher than that of the (100) plane, which means that  $\text{AuCl}_4^-$  at an appropriate concentration can be preferentially absorbed on (101) plane-forming Au NPs [34]. Figure 2B showed an XPS full spectrum from ZnO-Au sample, including the binding energy peaks of Zn, O, and Au. The detailed Zn (2p) spectrum (Figure 2C) revealed two peaks, which were assigned to the following groups: 2p<sub>1/2</sub> zinc peak at 1044.8 eV and 2p<sub>3/2</sub> zinc peak at 1021.7 eV with the separation distance of 23.1 eV, indicating the presence of Zn<sup>2+</sup> [27]. Figure 2D is the detailed O (1s) spectrum, which can be decomposed into two peaks located at 530.1 eV and 531.7 eV, respectively, indicating the presence of two different O in the material. The peak at 530.1 eV was attributed to the lattice oxygen of ZnO, while the peak at 531.7 eV belonged to the oxygen of the hydroxyl group (OH) on the surface of ZnO [21]. Figure 2E showed 83.1 eV and 86.9 eV corresponding to Au (4f<sub>7/2</sub>) and Au (4f<sub>5/2</sub>), respectively. Notably, the binding energy of Au (4f<sub>7/2</sub>) showed a negative shift of 0.9 eV compared with 84.0 eV of Au block [35], due to the electron transfer from ZnO



to Au [36]. XPS and XRD characterization further confirmed the successful synthesis of ZnO-Au composites for binding to the DNA.

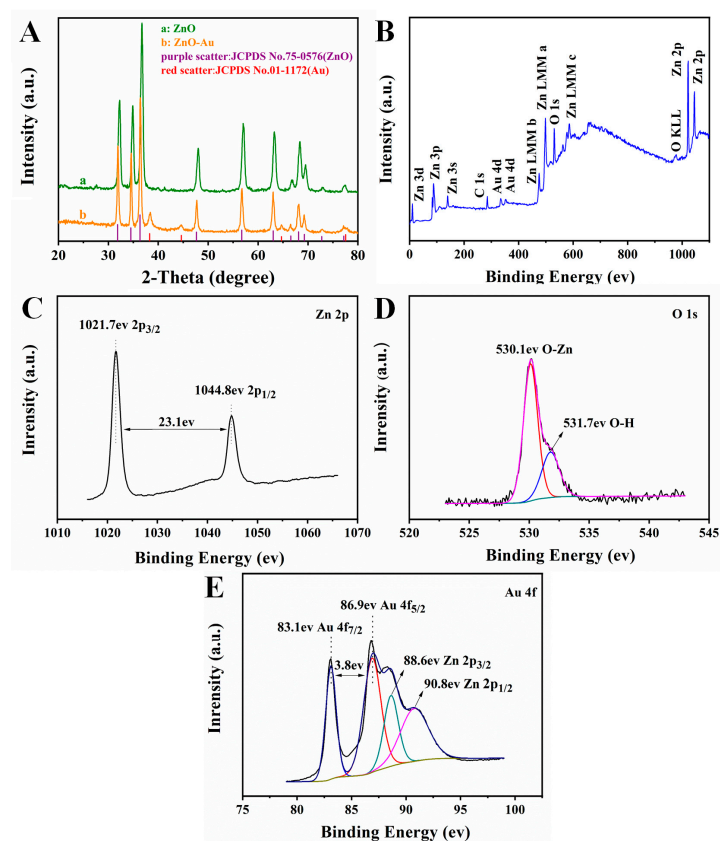


**Figure 2.** (A) XRD patterns of ZnO and ZnO-Au; (B) The full XPS spectrum; (C–E) Fine spectrum of XPS: Zn region, O region and Au region. The fitted peaks in regions (C–E) are performed by Gaussian fitting.

The stepwise modification of the electrochemical aptasensor was characterized using EIS (Figure S3B). Results showed that the EIS of ZnO (curve c) enlarged significantly with a bigger  $R_{ct}$ , compared with GCE (curve a). This result suggests that ZnO hinders the charge transfer from the redox probe of  $[\text{Fe}(\text{CN})_6]^{3-/4-}$  to the GCE surface due to the poor conductivity of ZnO. While for the Au–ZnO/GCE (curve b), an obvious decrease of the diameter of the semicircle ( $1654 \Omega$ ) was observed, implying that the existence of AuNPs could improve electrical conductivity and accelerate the electron transfer rate [37]. Previous study has shown that Au NPs formed on oxide supports are catalytically more active for oxidation reactions because of the polarization toward the support caused by Au NPs at the interface [38]. Then, the cDNA was bonded to the electrode by gold-sulfur bonds, leading to the increase of  $R_{ct}$  value ( $2114 \Omega$ ) due to the negative charge from the phosphate backbone of nucleic acid [39]. After MCH modification of the electrode the  $R_{ct}$  value ( $2340 \Omega$ ) increased, which indicated that the transfer of electroactive ions ( $[\text{Fe}(\text{CN})_6]^{3-/4-}$ ) to the electrode interface was impeded. The  $R_{ct}$  ( $3253 \Omega$ ) increased upon the complementation of Aptamer and cDNA to form double-stranded DNA. As one active substance, MB ( $R_{ct} = 2710 \Omega$ ) may facilitate the charge transfer [39]. However, after the modified electrode interacted with the OTA, the aptamer carrying OTA detached from the electrode surface and the  $R_{ct}$  value was reduced ( $2534 \Omega$ ). This phenomenon may be ascribed to the reduction of steric hindrance effect. It appeared that the changes of EIS demonstrate the success of each modification step.

### 3.3. Optimization

In order to improve the analytical performance of the electrochemical aptasensor, the incubation time of aptamer/MCH/cDNA/nafion@ZnO-Au/GCE in MB solution and the incubation time of MB/aptamer/MCH/cDNA/nafion@ZnO-Au/GCE in electrolyte containing OTA were investigated. As the incubation time of aptamer/MCH/cDNA/nafion@ZnO-Au/GCE in MB solution increases, the value of  $\Delta I = I_{OTA} - I_{no\ OTA}$  decreases gradually (Figure S4A). Therefore, 40 min was selected as the optimal incubation time for the modified electrode in MB solution. Analogously, 20 min was selected as the optimal incubation time for the functional electrode in electrolyte containing OTA (Figure S4B).

### 3.4. Analytical Performance

**Dynamic Range and Limit of Detection.** Under optimized conditions, DPV was used to detect the range of OTA concentrations ( $0\text{--}50,000\text{ pg}\cdot\text{mL}^{-1}$ ) due to its high sensitivity. In Figure 3A, the reduction peak current of MB gradually decreased as concentration OTA increased. Figure 3B showed a clear linear relationship between  $\Delta I$  and  $\lg C_{OTA}$  in the range of  $0.1\text{--}30,000\text{ pg}\cdot\text{mL}^{-1}$  with a detection limit of  $0.05\text{ pg}\cdot\text{mL}^{-1}$  ( $S/N = 3:1$ ). The linear regression equations were  $\Delta I (\mu\text{A}) = -0.2275 \lg C_{OTA} (\text{pg}\cdot\text{mL}^{-1}) - 1.0745$ , with the regression coefficient of 0.9993. The error percentages for each determination in Figure 3 were in the range of 94.3% to 108.4%. To further verify the proof of concept of the OTA sensing, fluorescence measurements during the capture of OTA by the aptamer and release of the OTA-aptamer conjugates were also designed. The aptamer and cDNA were modified with the BHQ2 quencher and Cy3 fluorophore, respectively. In the absence of OTA, BHQ2-aptamer is quenched by Cy3-cDNA, due to the formation of the double-strand DNA, and the fluorescence is turned off. In the presence of OTA, the BHQ2-aptamer capturing OTA releases from the double-strand DNA, causing the regeneration of fluorescence of the Cy3-cDNA. The fluorescence measurement showed that the fluorescence intensity in the solution increased along with the increasing OTA concentration (Figure 4A). The calibration curve of fluorescence intensity as a function of concentration ( $0\text{--}50,000\text{ pg}\cdot\text{mL}^{-1}$ ) was plotted. Figure 4B is the linear relationship between the fluorescence intensity and the logarithm of OTA concentration within the range of  $20\text{--}500\text{ nM}$  ( $R^2 = 0.990$ ). The calculated detection limit was  $16.5\text{ nM}$ . The above results further proved the flexibility of the proposed sensing concept and exhibited even better sensing ability for OTA determination.

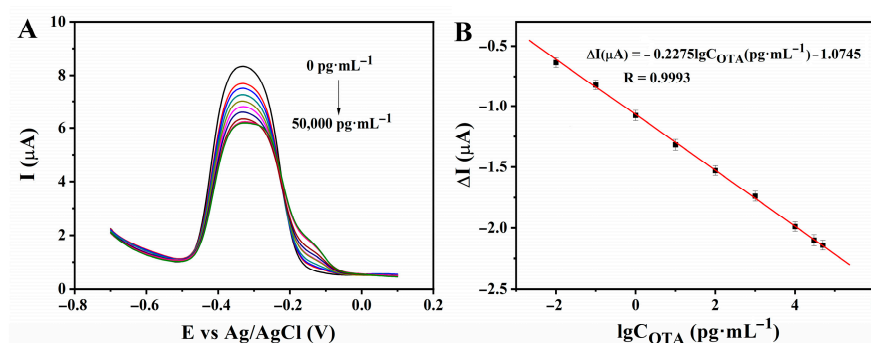


**Figure 3.** (A) Differential pulse voltammograms of a series of OTA concentrations ( $0, 0.01, 0.1, 1, 10, 100, 1000, 10,000, 30,000, 50,000\text{ pg}\cdot\text{mL}^{-1}$ ) using MB/Apt/MCH/cDNA/ZnO-Au/GCE were carried out under optimal conditions. (B) Calibration curve of anodic current ( $n = 5$ ) obtained from (A) showing a linear range from  $0.1$  to  $30,000\text{ pg}\cdot\text{mL}^{-1}$ .

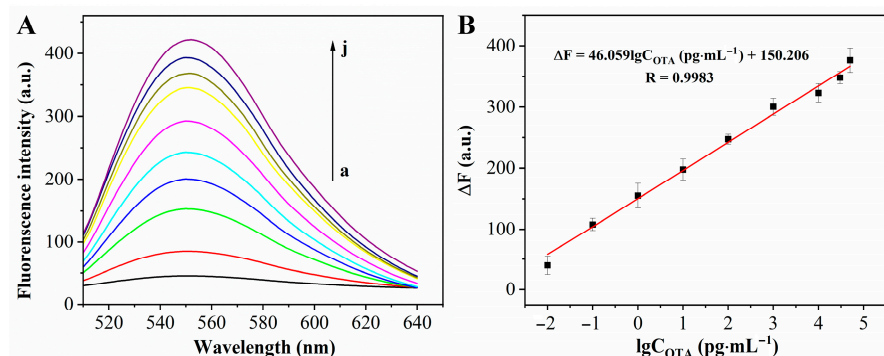


**Figure 4.** (A) Fluorescence spectra of the OTA-aptamer conjugates with different concentrations of OTA (0, 0.01, 0.1, 1, 10, 100, 1000, 10,000, 30,000, 50,000  $\text{pg}\cdot\text{mL}^{-1}$ ). (B) Calibration curve of  $\Delta F$  ( $n = 3$ ) obtained from (A) showing a linear range from 0.1 to 30,000  $\text{pg}\cdot\text{mL}^{-1}$ .

Compared with other OTA sensors, the analytical performance of the aptasensor was better than other kinds of methods for OTA determination (Table 1). Specially, the excellent sensitivity of the aptasensor was mainly attributed to the superior material utilized and electroactive molecules attached to nucleic acid structure. Some materials have been applied for the detection of OTA, such as carbon nanomaterials, metal-organic framework materials, quantum dots, metal/metal oxide nanomaterials, and upconversion nanomaterials (Table 1). Different types of materials have their own outstanding properties. Among these materials, ZnO-Au composites have outstanding properties with high specific surface area, easy functionalization, physicochemical stability, and high electronic conductivity that enable sensors based on this material to perform highly sensitive OTA analysis.

**Table 1.** List of the analytical performances of the proposed sensor with other kinds of methods for OTA determination.

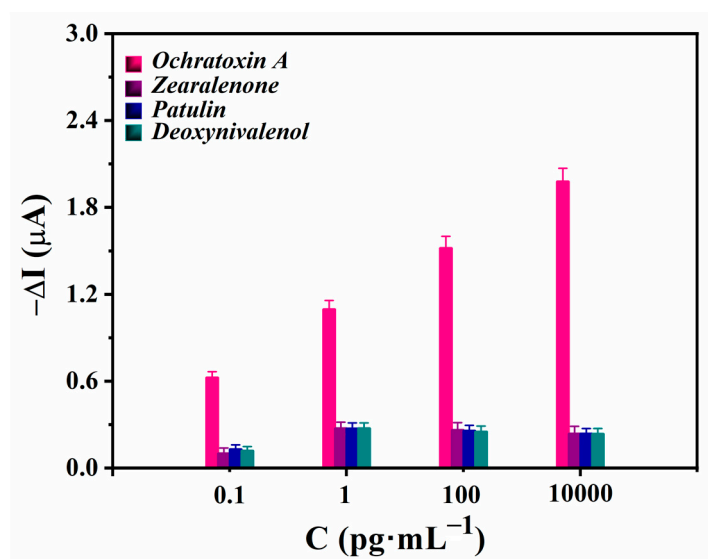
Detection Method	Material	Real Sample	Linear Range ( $\text{pg}\cdot\text{mL}^{-1}$ )	LOD ( $\text{pg}\cdot\text{mL}^{-1}$ )	Reference
LC	NA	Beer, wine, and juice	1000–50,000	25	[40]
UHPLC-MS/MS	NA	Tea	500–70,000,000	500	[41]
UHPLC-(ESI+)-MS/MS	NA	Coffee beverages	300–70,000	300	[42]
LC-MS/MS	NA	Pig and poultry matrices	250–250,000	1000	[43]
Chemiluminescence method	Anti-OTA antibodies-magnetic beads	Grains	5–405	2.05	[44]
Colorimetric method	G-quadruplex/hemin DNzyme	Rice	0.404–40.4	3.5	[45]
Surface-enhanced Raman spectroscopy	$\text{Fe}_3\text{O}_4$ NPs	Soybean, grape, and milk	40.4–16,160	12	[46]
Fluorescence method	UCNPs	Beer and wheat	5000–100,000	1860	[47]
Fluorescence method	Magnetic beads-exonuclease	Wheat and corn	500–75,000	28	[48]
Fluorescence and absorbance dual-mode immunoassay	G-quadruplex-TMB	Corn, oats, and rice	49–25,000	28	[49]
Electrochemiluminescence method	Au- $\text{CaCO}_3$ nanocomposites	Beer and wheat	10–100,000	5.7	[50]
Electrochemical method	Hairpin Aptamer	Wheat	1000–500,000	0.58	[51]
Electrochemical method	Aptamer-graphene oxide nanosheets	Wheat	10–50,000	5.6	[52]

Table 1. Cont.

Detection Method	Material	Real Sample	Linear Range (pg·mL <sup>-1</sup> )	LOD (pg·mL <sup>-1</sup> )	Reference
Electrochemical method	Aptamer-MoS <sub>2</sub>	Wine	0.5–1000	0.23	[53]
Electrochemical method	Aptamer-Au nanoparticles	NA	1–1000	0.5	[54]
Electrochemical method	OTA				
Electrochemical method	Antibody-palladium nanoparticles	Coffee	500–2000	96	[55]
Electrochemical method	GO-DNA complex	Oat and rice	0.01–1000	0.005	[56]
Electrochemical method	ZnO-Au composites	Wine & Beer	0.1–30,000	0.05	This work

LC: liquid chromatography. LC-MS/MS: liquid chromatography–triple quadrupole mass spectrometry. UHPLC-(ESI+)-MS/MS: ultra-high-pressure liquid chromatography/electrospray ionization tandem mass spectrometry. UHPLC-MS/MS: ultra-high-pressure liquid chromatography-mass spectrometry. Graphene oxide: GO. UCNPs: Upconversion nanoparticles. NA: not available.

The specificity is an extremely critical parameter for a designed aptasensor. To evaluate the specificity of the aptasensor, DPV was performed on the electrolyte (including OTA) with interference substances. ZEA, PAT, and DON were selected as interference substances due to reports that they coexist with OTA in food [39]. As shown in Figure 5, there was no significant signal in the presence of low concentration interference (0.1 pg·mL<sup>-1</sup>). The interference substances (>0.1 pg·mL<sup>-1</sup>) produced a constant signal background, which may be related to the low nonspecific recognition of the aptamer and the adsorption on the electrode surface. The interference substances (1 pg·mL<sup>-1</sup>) all produced less than 25% of the OTA signal. High concentrations (100 pg·mL<sup>-1</sup> or 10,000 pg·mL<sup>-1</sup>) of interfering substances produce less than 12% OTA signal. Therefore, we can guarantee that the biosensor is able to detect OTA in the presence of ZEA, PAT, and DON. Stability over time and repeatability are essential factors in the practical application of aptasensors. The functionalized electrodes were stored at 4 °C for 18 days to test the stability of the sensor. The developed biosensor can retain more than 92.6% of the initial response signal, which was probably due to the partial decomposition and conjugation of the aptamers on the electrode surface. In addition, five parallel experiments were performed to detect 1 pg·mL<sup>-1</sup> OTA for testing the repeatability of the sensing system. The relative standard deviation (RSD) was 3.8%, indicating the good repeatability of the biosensor. Due to aptamer specific capture OTA, the original dsDNA on the electrode is changed into ssDNA, thereby leading the regeneration of the cDNA linked ZnO-Au modified electrode. After that, the aptamer of the capture probe can once again bind to the cDNA-linked, ZnO-Au modified electrode for reuse. Results showed that the aptasensor only exhibited a slight downward trend in terms of performance after five times of reuse. The relative weak reproducibility and troublesome electron-transfer pathways of electrochemical sensing are still the main drawbacks that should be improved, especially for the application in complex food samples. However, it is expected that further miniaturization, including implantable devices, the functionalization of novel nanomaterials that contain more homogeneously binding sites with high affinity for the targets, as well as the combination of ink printing of nanomaterials, will solve the above challenges.



**Figure 5.**  $\Delta I$  values for the selectivity of the *Ochratoxin A* aptasensor against *zearalenone*, *patulin*, and *deoxynivalenol* for different concentrations.

To evaluate the feasibility of the sensing system, the modified electrode examined OTA in a real sample. We selected wine and beer that are susceptible to OTA infection during actual processing as actual samples. A series of concentrations of OTA (0.1–1000  $\text{pg}\cdot\text{mL}^{-1}$ ) were added to the processed samples for recovery experiments. The results of the recovery experiment are shown in Table 2. The recovery rate measured was in the range of 102.2–110%, and the RSD varied from 22.7% to 4.3%. It was worth noting that the recovery rate in actual samples was above 100%, which may be correlated with the nonspecific adsorption of the matrix. The results proved that this sensor can be used for OTA analysis in wine and beer samples. To further confirm the obtained accuracy and validity, the results were compared to the gold standard HPLC method and ELISA method. The recovery rate spiked samples for HPLC ranged from 98.6% to 103.8%, with an RSD of less than 4.0% (Table S1). Thus, the designed aptasensor enabled the effective quantitative detection of OTA in actual samples.

**Table 2.** Recovery Assay Data.

Spiked OTA ( $\text{pg}\cdot\text{mL}^{-1}$ )	Real Sample ( $\text{pg}\cdot\text{mL}^{-1}$ )		RSD ( $n = 5$ )		Recovery ( $n = 5$ )	
	Beverage 1	Beverage 2	Beverage 1	Beverage 2	Beverage 1	Beverage 2
0.1	0.11	0.106	3.8%	2.7%	110.0%	106.0%
1	1.095	1.05	3.6%	3.5%	109.1%	104.5%
100	105.2	106.0	3.4%	4.2%	105.2%	106.0%
1000	1022.0	1057.0	3.28	4.3%	102.2%	105.7%

Beverage 1: wine; Beverage 2: beer.  $n$ : number of measurements.

#### 4. Conclusions

In a nutshell, we designed an electrochemical biosensor reliant on ZnO-Au composites and targets induced the changes in the interaction between methylene blue and nucleic acids. The MB/aptamer/MCH/cDNA/nafion@ZnO-Au modified GCE provides high specific surface area, favorable conductivity, high selectivity, excellent sensitivity, long-term stability, and favorable repeatability. The biosensor has achieved OTA analysis in actual samples. Moreover, applications of this setup are not limited to OTA detection and are expected to be used as a template to detect other toxins.



**Supplementary Materials:** The following supporting information can be downloaded at: <https://www.mdpi.com/article/10.3390/pr11030864/s1>, Figure S1: The CV curves at different scanning rates from 10 to 200 mV s<sup>-1</sup> for the prepared electrode (A) before and (B) after the release of MB. (C) Plots of peak currents vs. scan rates corresponding to (A). (D) Plots of peak currents vs. square root of scan rates corresponding to (B); Figure S2: UV-visible absorption spectra of MB: (a) 10 μM pure MB, (b) after incubation with 10 μM MB and 0.5 μM dsDNA, (c) after incubation with 10 μM MB and 0.5 μM ssDNA; Figure S3: (A) Electrochemical impedance spectroscopy for bare GCE, ZnO-Au/GCE, and ZnO/GCE (a–c) in 1.0 mM [Fe(CN)<sub>6</sub>]<sup>-3/-4</sup> + 0.1 M KCl solution through applying initial potential of 0.27 V vs Ag/AgCl reference electrode and an amplitude of 5 mV in a frequency range of 10<sup>-2</sup>–10<sup>5</sup> Hz. The insertion diagram is an equivalent circuit model of the EIS analysis. (B) Electrochemical impedance spectroscopy after each fabrication step recorded: (a') ZnO-Au/GCE, (b') nafion/ZnO-Au/GCE, (c') cDNA/nafion/ZnO-Au/GCE, (d') MCH/cDNA/nafion/ZnO-Au/GCE, (e') OTA/MB/aptamer/(d'), (f') MB/aptamer/(d'), (g') aptamer/(d').; Figure S4: Optimization experiment of (A) incubation time of aptamer/MCH/cDNA/nafion@ZnO-Au/GCE in 20 μM MB and (B) incubation time of MB/aptamer/MCH/cDNA/nafion@ZnO-Au/GCE in 0.1 pg·mL<sup>-1</sup> OTA; Table S1: Recovery assay data of electrochemical aptasensor, HPLC and ELISA.

**Author Contributions:** Writing, investigation, original draft preparation, S.Z.; investigation and discussion, Y.W. revision, supervision, discussion and project administration, T.Y. and Q.S. All authors have read and agreed to the published version of the manuscript.

**Funding:** This work was financially supported by the National Key Research and Development Program of China (2019YFC1606703, Ministry of Science and Technology of China), the Education Department of Shaanxi Province (22JK0354, Education Department of Shaanxi Province, China), Youth Talent Lift Program of Shaanxi Association for Science and technology (20220320, Education Department of Shaanxi Province, China), Subject Innovation Team of Shaanxi University of Chinese Medicine (2019-YL10, Shaanxi University of Chinese Medicine, China), the Natural Science Foundation of Shaanxi Province (2023-YBSF-245, Shaanxi Science and Technology Department, China).

**Data Availability Statement:** Not applicable.

**Conflicts of Interest:** The authors declare no competing financial interest.

## References

1. Li, X.J.; Ma, W.; Ma, Z.Y.; Zhang, Q.H.; Li, H.M. Recent progress in determination of ochratoxin A in foods by chromatographic and mass spectrometry methods. *Crit. Rev. Food Sci. Nutr.* **2021**, *13*, 1–32. [[CrossRef](#)] [[PubMed](#)]
2. Heussner, A.H.; Bingle, L.E.H. Comparative ochratoxin toxicity: A review of the available data. *Toxins* **2015**, *7*, 4253–4282. [[CrossRef](#)] [[PubMed](#)]
3. Singh, A.K.; Lakshmi, G.B.V.S.; Dhiman, T.K.; Kaushik, A.; Solanki, P.R. Bio-Active free direct optical sensing of aflatoxin B<sub>1</sub> and ochratoxin A using a manganese oxide nano-system. *Front. Nanotechnol.* **2021**, *2*, 621681. [[CrossRef](#)]
4. GB 2761-2017; National Standards of the People's Republic of China. Mycotoxins in Food Limited. Standards Press of China: Beijing, China, 2017.
5. Alizadeh, N.; Hashemi, J.; Shahdost-Fard, F. Spectrofluorimetric study of the complexation of ochratoxin A and Cu<sup>2+</sup>: Towards the hybrid fluorimetric sensor and visual detection of ochratoxin A in wheat flour samples from farm to fork. *Food Chem.* **2021**, *350*, 129204. [[CrossRef](#)] [[PubMed](#)]
6. Moez, E.; Noel, D.; Brice, S.; Benjamin, G.; Pascaline, A.; Didier, M. Aptamer assisted ultrafiltration cleanup with high performance liquid chromatography-fluorescence detector for the determination of OTA in green coffee. *Food Chem.* **2020**, *310*, 125851. [[CrossRef](#)]
7. Liu, X.; Tang, Z.W.; Duan, Z.H.; He, Z.Y.; Shu, M.; Wang, X.X.; Gee, S.J.; Hammock, B.D.; Xu, Y. Nanobody-based enzyme immunoassay for ochratoxin A in cereal with high resistance to matrix interference. *Talanta* **2017**, *164*, 154–158. [[CrossRef](#)]
8. Yuan, W.; Lu, L.X.; Lu, Y.C.; Xiong, X.; Li, Y.; Cui, X.W.; Liu, Y.J.; Xiong, X.H. Synergistic effects of DNA structure for ultrasensitive detecting OTA in grains. *Food Anal. Methods* **2021**, *14*, 2308–2316. [[CrossRef](#)]
9. Thévenot, D.R.; Toth, K.; Durst, R.A.; Wilson, G.S. Electrochemical biosensors: Recommended definitions and classification. *Biosens. Bioelectron.* **2001**, *16*, 121–131. [[CrossRef](#)]
10. Beluomini, M.A.; Silva, J.L.; Sá, A.C.D.; Buffon, E.; Pereira, T.C.; Stradiotto, N.R. Electrochemical sensors based on molecularly imprinted polymer on nanostructured carbon materials: A review. *J. Electroanal. Chem.* **2019**, *840*, 343–366. [[CrossRef](#)]
11. Sun, X.F.; Chen, H.H.; Wang, S.L.; Zhang, Y.P.; Tian, Y.P.; Zhou, N.D. Electrochemical detection of sequence-specific DNA based on formation of G-quadruplex-hemin through continuous hybridization chain reaction. *Anal. Chim. Acta* **2018**, *1021*, 121–128. [[CrossRef](#)]

12. Zhao, K.; Quan, X. Carbon-based materials for electrochemical reduction of CO<sub>2</sub> to C<sub>2+</sub> oxygenates: Recent progress and remaining challenges. *ACS Catal.* **2021**, *11*, 2076–2097. [[CrossRef](#)]
13. Daviddi, E.; Chen, Z.; Massani, B.B.; Lee, J.; Bentley, C.L.; Unwin, P.R.; Ratcliff, E.L. Nanoscale visualization and multiscale electrochemical analysis of conductive polymer electrodes. *ACS Nano* **2019**, *13*, 13271–13284. [[CrossRef](#)]
14. Chen, S.B.; Yuan, B.Q.; Liu, G.; Zhang, D.J. Electrochemical sensors based on covalent organic frameworks: A critical review. *Front. Chem.* **2020**, *8*, 601044. [[CrossRef](#)] [[PubMed](#)]
15. Sun, Y.; Li, Y.X.; Wang, N.; Xu, Q.Q.; Xu, L.; Lin, M. Copper-based metal-organic framework for non-enzymatic electrochemical detection of glucose. *Electroanalysis* **2018**, *30*, 474–478. [[CrossRef](#)]
16. Hu, R.; Zhang, X.; Chi, K.N.; Yang, T.; Yang, Y.H. Bifunctional MOFs-based ratiometric electrochemical sensor for multiplex heavy metal ions. *ACS Appl. Mater. Interfaces* **2020**, *12*, 30770–30778. [[CrossRef](#)] [[PubMed](#)]
17. Sharma, A.; Ahmed, A.; Singh, A.; Oruganti, S.K.; Khosla, A.; Arya, S. Review-recent advances in tin oxide nanomaterials as electrochemical/chemiresistive sensors. *J. Electrochem. Soc.* **2021**, *168*, 027505. [[CrossRef](#)]
18. Prathap, M.U.A.; Kaur, B.; Srivastava, R. Electrochemical sensor platforms based on nanostructured metal oxides, and zeolite-based materials. *Chem. Rec.* **2019**, *19*, 883–907. [[CrossRef](#)]
19. Ortiz-Casas, B.; Galdámez-Martínez, A.; Gutiérrez-Flores, J.; Ibañez, A.B.; Panda, P.K.; Santana, G.; Vega, H.A.D.L.; Suar, M.; Rodelo, C.G.; Kaushik, A.; et al. Bio-acceptable 0D and 1D ZnO nanostructures for cancer diagnostics and treatment. *Mater. Today* **2021**, *50*, 533–569. [[CrossRef](#)]
20. Das, S.; Mukhopadhyay, S.; Chatterjee, S.; Devi, P.S.; Kumar, G.S. Fluorescent ZnO-Au nanocomposite as a probe for elucidating specificity in DNA interaction. *ACS Omega* **2018**, *3*, 7494–7507. [[CrossRef](#)]
21. Mahajan, H.; Bae, J.; Yun, K. Facile synthesis of ZnO-Au nanocomposites for high-performance supercapacitors. *J. Alloys Compd.* **2018**, *758*, 131–139. [[CrossRef](#)]
22. Yao, C.J.; Lin, J.M.; Wu, L.; Li, L.Q.; Xu, N.; Sun, J.; Wu, J.D. High visible light photocatalytic activity of ZnO-Au nanocomposites synthesized by a controlled hydrothermal method. *Phys. Status Solidi (A) Appl. Mater. Sci.* **2021**, *218*, 2100150. [[CrossRef](#)]
23. Ilgu, M.; Nilsen-Hamilton, M. Aptamers in analytics. *Analyst* **2016**, *141*, 1551–1568. [[CrossRef](#)]
24. Röthlisberger, P.; Hollenstein, M. Aptamer chemistry. *Adv. Drug Deliv. Rev.* **2018**, *134*, 3–21. [[CrossRef](#)]
25. Zhao, H.Y.; Qiao, X.J.; Zhang, X.L.; Niu, C.; Yue, T.L.; Sheng, Q.L. Simultaneous electrochemical aptasensing of patulin and ochratoxin A in apple juice based on gold nanoparticles decorated black phosphorus nanomaterial. *Anal. Bioanal. Chem.* **2021**, *413*, 3131–3140. [[CrossRef](#)]
26. Pica, A.; Krauss, I.R.; Parente, V.; Tateishi-Karimata, H.; Nagatoishi, S.; Tsumoto, K.; Sugimoto, N.; Sica, F. Through-bond effects in the ternary complexes of thrombin sandwiched by two DNA aptamers. *Nucleic Acids Res.* **2017**, *45*, 461–469. [[CrossRef](#)] [[PubMed](#)]
27. Wang, X.J.; Wang, W.; Liu, Y.L. Enhanced acetone sensing performance of Au nanoparticles functionalized flower-like ZnO. *Sens. Actuators B Chem.* **2012**, *168*, 39–45. [[CrossRef](#)]
28. Tabrizi, M.A.; Ferré-Borrull, J.; Marsal, L.F. Remote sensing of Salmonella-specific DNA fragment by using nanoporous alumina modified with the single-strand DNA probe. *Sens. Actuators B* **2020**, *304*, 127302. [[CrossRef](#)]
29. Mudasir; Wahyuni, E.T.; Tjahjono, D.H.; Yoshioka, N.; Inoue, H. Spectroscopic studies on the thermodynamic and thermal denaturation of the ct-DNA binding of methylene blue. *Spectrochim. Acta Part A Mol. Biomol. Spectrosc.* **2010**, *77*, 528–534. [[CrossRef](#)]
30. Palinska, A.; Grodzka, A.; Elzanowska, H.; Kepska, B.; Zwierkowska, E.; Achmatowicz, S.; Maj-Zurawska, M. Methylene blue interactions with chromosomal and plasmid DNA on screen-printed carbon electrodes. *Electroanalysis* **2010**, *22*, 1306–1313. [[CrossRef](#)]
31. Han, N.S.; Kim, D.H.; Lee, J.W.; Kim, J.; Shim, H.S.; Lee, Y.J.; Lee, D.; Song, J.K. Unexpected size effect observed in ZnO-Au composite photocatalysts. *ACS Appl. Mater. Interfaces* **2016**, *8*, 1067–1072. [[CrossRef](#)]
32. Wang, M.K.; Shen, Y.; Liu, Y.; Wang, T.; Zhao, F.; Liu, B.F.; Dong, S.J. Direct electrochemistry of microperoxidase 11 using carbon nanotube modified electrodes. *J. Electroanal. Chem.* **2005**, *578*, 121–127. [[CrossRef](#)]
33. Pillai, R.; Preetha, S.; Narasimhamurthy, B.; Lekshmi, I.C. Biosensing of catechol via amperometry using laccase immobilized nickel oxide/graphite modified screen-printed electrodes. *Mater. Today Proc.* **2022**, *62*, 5434–5438. [[CrossRef](#)]
34. Kochuveedu, S.T.; Oh, J.H.; Do, Y.R.; Kim, D.H. Surface-plasmon-enhanced band emission of ZnO nanoflowers decorated with Au nanoparticles. *Chem. Eur. J.* **2012**, *18*, 7467–7472. [[CrossRef](#)] [[PubMed](#)]
35. Zhang, J.; Liu, X.H.; Wang, L.W.; Yang, T.L.; Guo, X.Z.; Wu, S.H.; Wang, S.R.; Zhang, S.M. Au-functionalized hematite hybrid nanospindles: General synthesis, gas sensing and catalytic properties. *J. Phys. Chem. C* **2011**, *115*, 5352–5357. [[CrossRef](#)]
36. Liu, X.H.; Zhang, J.; Wang, L.W.; Yang, T.L.; Guo, X.Z.; Wu, S.H.; Wang, S.R. 3D hierarchically porous ZnO structures and their functionalization by Au nanoparticles for gas sensors. *J. Mater. Chem.* **2011**, *21*, 349–356. [[CrossRef](#)]
37. Fang, L.X.; Huang, K.J.; Zhang, B.L.; Liu, Y.J.; Zhang, Q.Y. A label-free electrochemistry biosensor based flower-like 3-dimensional ZnO superstructures for detection of DNA arrays. *New J. Chem.* **2014**, *38*, 5918–5924. [[CrossRef](#)]
38. Liu, X.W. Selective growth of Au nanoparticles on (111) facets of Cu<sub>2</sub>O microcrystals with an enhanced electrocatalytic property. *Langmuir* **2011**, *27*, 9100–9104. [[CrossRef](#)]
39. Rivas, L.; Mayorga-Martinez, C.C.; Quesada-Gonzalez, D.; Zamora-Gálvez, A.; Escosura-Muñiz, A.D.L.; Merkoçi, A. Label-free impedimetric aptasensor for ochratoxin-A detection using iridium oxide nanoparticles. *Anal. Chem.* **2015**, *87*, 5167–5172. [[CrossRef](#)]

40. Cao, J.L.; Kong, W.J.; Zhou, S.J.; Yin, L.H.; Wan, L.; Yang, M.H. Molecularly imprinted polymer-based solid phase clean-up for analysis of ochratoxin A in beer, red wine, and grape juice. *J. Sep. Sci.* **2013**, *36*, 1291–1297. [[CrossRef](#)]
41. Cina, M.; Ponce, M.D.; Martinez, L.D.; Cerutti, S. Development of a novel UHPLC-MS/MS method for the determination of ochratoxin A in tea. *Heliyon* **2021**, *7*, e06663. [[CrossRef](#)]
42. Cina, M.; Ponce, M.D.V.; Fernandez, L.; Cerutti, S. A green approach for Ochratoxin A determination in coffee infusions. *J. Food Comp. Anal.* **2022**, *114*, 104777. [[CrossRef](#)]
43. Streit, B.; Czabany, T.; Weingart, G.; Marchetti-Deschmann, M.; Prasad, S. Toolbox for the Extraction and Quantification of Ochratoxin A and Ochratoxin Alpha Applicable for Different Pig and Poultry Matrices. *Toxins* **2022**, *14*, 432. [[CrossRef](#)] [[PubMed](#)]
44. Zhang, B.; Liu, W.T.; Liu, Z.J.; Fu, X.L.; Du, D.L. Establishment of a Chemiluminescence Immunoassay Combined with Immunomagnetic Beads for Rapid Analysis of Ochratoxin A. *J. Aoac. Int.* **2022**, *105*, 346–351. [[CrossRef](#)]
45. Li, D.Y.; Xia, H.Y.; Sun, Y.Y.; Liu, W.J.; Liu, W.; Yu, J.N.; Jing, G.X.; Zhang, J.; Li, W.S. Colorimetric aptasensor for the sensitive detection of ochratoxin A based on a triple cascade amplification strategy. *Anal. Chim. Acta* **2022**, *1237*, 340616. [[CrossRef](#)] [[PubMed](#)]
46. Wang, H.; Chen, L.; Li, M.; She, Y.X.; Zhu, C.; Yan, M.M. An Alkyne-Mediated SERS Aptasensor for Anti-Interference Ochratoxin A Detection in Real Samples. *Foods* **2022**, *11*, 3407. [[CrossRef](#)]
47. Wu, S.; Liu, L.; Duan, N.; Wang, W.; Yu, Q.; Wang, Z. A test strip for ochratoxin A based on the use of aptamer-modified fluorescence upconversion nanoparticles. *Microchim. Acta* **2018**, *185*, 497. [[CrossRef](#)]
48. Liu, M.; Liu, S.; Ma, Y.; Li, B. Construction of a fluorescence biosensor for ochratoxin A based on magnetic beads and exonuclease III-assisted DNA cycling signal amplification. *Anal. Methods* **2022**, *14*, 734–740. [[CrossRef](#)]
49. Xiao, Y.; Zhang, X.P.; Ma, L.Y.; Fang, H.J.; Yang, H.L.; Zhou, Y. Fluorescence and absorbance dual-mode immunoassay for detecting Ochratoxin A. *Spectrochim. Acta A Mol. Biomol. Spectrosc.* **2022**, *279*, 121440. [[CrossRef](#)]
50. Li, L.; Liu, X.; He, S.; Cao, H.; Su, B.; Huang, T.; Chen, Q.; Liu, M.; Yang, D.P. Electrochemiluminescence Immunosensor Based on Nanobody and Au/CaCO<sub>3</sub> Synthesized Using Waste Eggshells for Ultrasensitive Detection of Ochratoxin A. *ACS Omega* **2021**, *6*, 30148–30156. [[CrossRef](#)] [[PubMed](#)]
51. Liu, C.; Guo, Y.; Luo, F.; Rao, P.; Fu, C.; Wang, S. Homogeneous Electrochemical Method for Ochratoxin A Determination Based on Target Triggered Aptamer Hairpin Switch and Exonuclease III-Assisted Recycling Amplification. *Food Anal. Methods* **2017**, *10*, 1982–1990. [[CrossRef](#)]
52. Sun, A.L.; Zhang, Y.F.; Sun, G.P.; Wang, X.N.; Tang, D. Homogeneous electrochemical detection of ochratoxin A in foodstuff using aptamer-graphene oxide nanosheets and DNase I-based target recycling reaction. *Biosens. Bioelectron.* **2017**, *89*, 659–665. [[CrossRef](#)] [[PubMed](#)]
53. Tang, J.; Huang, Y.; Cheng, Y.; Huang, L.; Zhuang, J.; Tang, D. Two-dimensional MoS<sub>2</sub> as a nano-binder for ssDNA: Ultrasensitive aptamer based amperometric detection of Ochratoxin A. *Microchim. Acta* **2018**, *185*, 162. [[CrossRef](#)] [[PubMed](#)]
54. Wang, X.Y.; Shan, Y.Q.; Gong, M.; Jin, X.; Lv, L.; Jiang, M.; Xu, J. A novel electrochemical sensor for ochratoxin A based on the hairpin aptamer and double report DNA via multiple signal amplification strategy. *Sens. Actuators B* **2019**, *281*, 595–601. [[CrossRef](#)]
55. Kunene, K.; Weber, M.; Sabela, M.; Voiry, D.; Kanchi, S.; Bisetty, K.; Bechelany, M. Highly-efficient electrochemical label-free immunosensor for the detection of ochratoxin A in coffee samples. *Sens. Actuators B* **2020**, *305*, 127438. [[CrossRef](#)]
56. Hu, Y.; Xie, H.Y.; Hu, J.Y.; Yang, D.T. Disposable electrochemical aptasensor based on graphene oxide-DNA complex as signal amplifier towards ultrasensitive detection of ochratoxin A. *Micromachines* **2022**, *13*, 834. [[CrossRef](#)]

**Disclaimer/Publisher’s Note:** The statements, opinions and data contained in all publications are solely those of the individual author(s) and contributor(s) and not of MDPI and/or the editor(s). MDPI and/or the editor(s) disclaim responsibility for any injury to people or property resulting from any ideas, methods, instructions or products referred to in the content.